PHYSICAL REVIEW B VOLUME 57, NUMBER 8 15 FEBRUARY 1998-II

Valence-band energy-momentum densities of amorphous SiO_2 by $(e,2e)$ spectroscopy

Z. Fang, X. Guo, S. A. Canney, S. Utteridge, M. J. Ford, and I. E. McCarthy
Electronic Structure of Materials Centre, The Flinders University of South Australia, Adelaide, SA 5001, Australia

A. S. Kheifets, M. Vos, and E. Weigold
Research School of Physical Sciences and Engineering, The Australian National University, Canberra, ACT 0200, Australia

(Received 28 July 1997)

We have measured the energy-momentum density of amorphous silicon dioxide using an $(e,2e)$ spectrometer with 20.8 keV incident, 19.6 keV scattered, and 1.2-keV ejected electron energies. The amorphous SiO_2 sample was prepared by oxidizing a thin silicon membrane. The experimental data show a valence electronic structure characteristic of upper p-like and lower s-like bands. The width of the upper valence band is 10 eV. This is separated by 9 eV from the lower valence band, which exhibits 2-eV dispersion. We have calculated the energy-momentum density of α-quartz using the *ab initio* linear muffin-tin orbital method and the result is spherically averaged over all crystal directions to enable comparison with the experiment. The calculated electron momentum densities show very good agreement with experiment for both the upper and lower valence bands. The theoretical prediction of the energy separation between the upper and lower valence bands is about 2 eV smaller than that measured and this discrepancy is discussed. The agreement between theory and experiment suggests that the short-range order in silicon dioxide plays an important role in determining the electronic structure of this material. [S0163-1829(98)04908-X]

I. INTRODUCTION

$(e,2e)$ spectroscopy is a powerful technique for measuring the electron energy-momentum densities in both gaseous[1] and solid[2] targets. In an $(e,2e)$ reaction an incident electron of well-defined momentum and energy ejects an electron from the target and the two outgoing electrons (scattered and ejected) are subsequently detected in coincidence. The binding-energy ε and momentum $\mathbf{q}$ of the target electron before the collision are then determined by conservation of energy and momentum. At sufficiently high incident energy and large momentum transfer the $(e,2e)$ process can be treated using the plane-wave approximation,[1,3] which leads to an $(e,2e)$ cross section proportional to the energy-momentum density $|\phi(\varepsilon,\mathbf{q})|^2$ of the target electrons. Since the measured $(e,2e)$ intensity depends only on the factor $|\phi(\varepsilon,\mathbf{q})|^2$ and the experimental conditions, one can apply the $(e,2e)$ technique equally well to amorphous, disordered, or crystalline materials. This contrasts sharply with the photoemission technique[4] that is applied more successfully to crystalline materials. In the past few years we have performed a series of $(e,2e)$ measurements on structurally disordered materials including amorphous carbon,[5] amorphous silicon,[6] silicon carbide,[7] copper,[8] aluminum,[9] and aluminum oxide.[10] Recently, $(e,2e)$ studies on single crystalline materials (graphite and silicon) have also been carried out. These experiments demonstrate that electron-momentum spectroscopy based on the $(e,2e)$ reaction can directly measure the electron-momentum distributions and visualize the dispersion relation between the binding energy and momentum of electrons in solids.

The electronic structure of silicon dioxide has been an interesting subject for many years. Silicon dioxide is a material widely used in industries from traditional glass making to modern semiconductor device fabrication. Pure SiO_2 plays an important role in the optical fiber manufacturing industry. Despite being a common and familiar material, studies of the electronic structure of silicon dioxide have been a challenge to both theoreticians and experimentalists. Calculations based on semiempirical models are often used to interpret experimental observations. Amongst the few *ab initio* solid-state calculations for the electronic properties of silicon dioxide[11–17] there is little or no attention paid to the momentum densities of the valence electrons. The difficulties in the theoretical analysis are related to the complexity of the SiO_2 system. Natural silica, which is one of the principal constituents of Earth's mantle, exists in a multitude of allotropic forms with more than 35 crystalline polymorphs known.[18] The crystal structure of most, but not all, of these polymorphs are well determined.[19] Recent studies on β-cristobalite[20] have indicated that it has a rather complicated structure instead of the simple cubic structure suggested by Wyckoff.[19] Because of its simplicity the cubic β-cristobalite structure has been frequently used[14,21] as a model crystal for SiO_2 and discrepancies between theory and experiment are significant.

Experiments using ultraviolet-photoemission spectroscopy, x-ray photoemission spectroscopy (XPS) and x-ray-absorption and emission spectroscopy are able to accurately measure the energy levels of the valence band.[22–27] It is known that photoemission cross sections depend on the electron state; therefore the emission spectrum cannot be compared directly with the calculated density of states (DOS). Optical absorption measurements,[28,29] which probe the top of the valence band and the conduction band, are often complicated by excitons[14] and other experimental difficulties not directly related to the band structure. All of these experiments cannot reveal information regarding electron-momentum densities. $(e,2e)$ spectroscopy, however, gives the energy-resolved electron-momentum density that provides more detailed information than the DOS measure-

0163-1829/98/57(8)/4349(9)/$15.00

ments. There are no extra enhancement effects in the $(e,2e)$ measurement and the comparison with theory is straightforward.

In this paper we present our recent $(e,2e)$ measurement on the valence-band electronic structure of amorphous SiO_2. We carry out an *ab initio* linear muffin-tin orbital (LMTO) calculation on α-quartz and use the spherically averaged result to compare and analyze the experimental data. The LMTO calculation is described in Sec. II; in Sec. III we give sample preparation details and experimental setup. The measured and calculated energy-momentum densities are compared and discussed in Sec. IV, together with a brief comparison to our earlier $(e,2e)$ measurement on aluminum oxide. We conclude our observations in Sec. V.

II. LMTO CALCULATION

Disordered forms of SiO_2 have been studied previously using computational methods making no specific use of the long-range crystalline order.[30] We have adopted another approach and calculate the band structure and energy-momentum density of the oriented crystal. For this purpose, we have employed the LMTO method,[31] which has the advantages of sufficiently high accuracy and computational efficiency suitable for a complex material like SiO_2. In our model the exchange and correlation terms of the many-electron Hamiltonian are treated in the local-density approximation of the density-functional theory. To describe the disordered form of SiO_2 the energy-momentum density obtained from the crystalline calculation is spherically averaged to remove the vector property of the momentum.[32] All directions in the momentum space therefore become equivalent. Although this is a somewhat idealized scheme for describing a randomly oriented polycrystalline material, it turns out to be a useful approximation to the electronic structure of disordered materials.[5–10]

We choose α-quartz as the prototype crystal to perform the LMTO calculation. At room temperature and ambient pressure α-quartz is the only crystal structure thermodynamically stable. The crystal structure of α-quartz is well known[19,33] and many theoretical and experimental studies have focused on this material. Although silica exists in many allotropic forms the most common ones, including α-quartz, are built from the SiO_4 tetrahedral unit. In these materials each silicon atom is coordinated by four oxygen atoms and each oxygen atom is bounded by two silicon atoms (4:2 coordinated) and interconnects two SiO_4 units. It is known that the difference in electronic structure between various SiO_2 polymorphs is quite small. In α-quartz the SiO_4 unit is very close to an ideal tetrahedron as all the O-Si-O angles are around 109° and the Si-O bond length is 1.61 Å. The Si-O-Si angle varies according to the crystal structure and in α-quartz this angle is around 144°. The SiO_4 tetrahedron is quite stable and similar short-range order also exists in amorphous SiO_2. The O-Si-O angle in thermally oxidized silicon is found[27] to vary between 100°–112° with a maximum at 109° and the mean length of the Si-O bond is $1.60\ \text{Å} \pm 10\%$. The dihedral Si-O-Si angle is however distributed in the 120°–180° range with a maximum at 142°–144°. In this picture one can view the structure of amorphous SiO_2 as a network of SiO_4 tetrahedrons connected at the O corners. The long-range order is lost but the short-range order, which exists in all 4:2 coordinated SiO_2 systems, should have a significant influence on the electronic structure of the material.

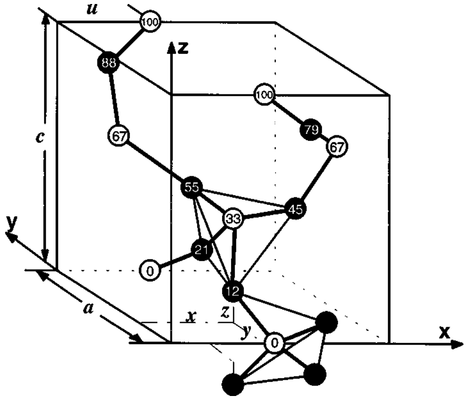

FIG. 1. The left-handed α-quartz structure where the Si and O atoms are represented by white and black circles, respectively. The relative height (z coordinate) of each atom is indicated by the number inside the circle. Two SiO_4 tetrahedrons connected by the O_{12} atom are highlighted. Notice the empty space near the origin and volume center.

The unit cell of α-quartz is shown in Fig. 1. There are three Si and six O atoms in the hexagonal cell. The non-equivalent atomic positions are chosen to have the following coordinates:

$$\mathrm{Si}_0\ (u,0,0),\quad \mathrm{Si}_{33}\ (1-u,1-u,\tfrac{1}{3}),\quad \mathrm{Si}_{67}\ (0,u,\tfrac{2}{3}),$$

$$\mathrm{O}_{12}\ (x,y,z),\quad \mathrm{O}_{21}\ (1-x,1+y-x,\tfrac{1}{3}-z),$$

$$\mathrm{O}_{45}\ (1+y-x,1-x,z+\tfrac{1}{3}),\quad \mathrm{O}_{55}\ (y,x,\ \tfrac{2}{3}-z),$$

$$\mathrm{O}_{79}\ (1-y,x-y,z+\tfrac{2}{3}),\quad \mathrm{O}_{88}\ (x-y,1-y,1-z).$$

A left-handed threefold screw axis exists in the sequences of Si and two groups of O atoms. The hexagonal lattice constants (a,c) and four internal parameters (u,x,y,z) are given in Table I. We use the parameters for left-handed quartz (Fig. 1 with D_3^4 symmetry) given by Wyckoff.[19] Levien, Prewitt and Weidner[33] reported the crystallographic data for right-handed quartz (D_3^6 symmetry) with similar values. In natural crystals both forms often coexist. We believe the difference in the electronic structure for different symmetries is negligible.

From Fig. 1 it is obvious that there are no significant empty regions near the origin and the center of the unit cell. To treat such an open structure using the LMTO method we have to introduce a number of fictitious “empty” atoms. Starting from the origin and applying the screw operation we get a sequence of empty atoms:

$$E_0(\delta,\varepsilon,\gamma),\quad E_{33}(\varepsilon-\delta,-\delta,\gamma+\tfrac{1}{3}),$$

$$E_{66}(-\varepsilon,\delta-\varepsilon,\gamma+\tfrac{2}{3}),$$

and similarly to fill the volume center we get another sequence:

TABLE I. Unit-cell constants and internal parameters for α-quartz with D_3^4 symmetry shown in Fig. 1. The parameters for the ''empty atoms'' are described in the text.

Unit cell constants: $a=4.913$ Å, $c=5.405$ Å

Parameter for Si and O atoms		Parameter for empty atoms	
u	0.465	δ	-0.083
x	0.415	ε	0.095
y	0.272	γ	0.105
z	0.120	v	0.346

$$E_{16}(0,v,\tfrac{1}{6}),\quad E_{50}(v,0,\tfrac{1}{2}),\quad E_{84}(1-v,1-v,\tfrac{5}{6}).$$

The parameters ε, δ, γ, and v are given in Table I. A detailed procedure of finding optimal positions for these empty spheres and calculating their radii is described in Ref. 34. Restricting ourselves to the atomic-sphere approximation, we equate the total volume of the atomic spheres to the volume of the unit cell and discard the interstitial region. The six empty atoms together with the Si and O atoms contribute to one s and three p orbitals that form the LMTO basis. The d orbitals are downfolded and do not change the size of the basis.

The band structure and DOS of α-quartz calculated using the LMTO method are shown in Fig. 2. The band energies obtained from several self-consistent band-structure calculations are compared in Table II. Our energy bands and DOS are consistent with other theoretical calculations. It can be seen that the valence-band structure of α-quartz consists of three distinct groups of bands separated in energy. The uppermost 12 bands in the upper valence band ($\mathrm{UVB_I}$) are formed by O $2p$-like nonbinding orbitals with low dispersion (3.3 eV). The next six bands ($\mathrm{UVB_{II}}$) are predominantly composed of O $2p$-like and Si sp bonding states. The lowest six bands (LVB) basically consist of O $2s$-like states with a dispersion of 2.7 eV. The LMTO calculation also indicates an indirect gap of about 6.6 eV occurring between valence maximum at K and conduction-band minimum at Γ. Like other recent local-density calculations,[14,16] this result significantly underestimates the experimental value (8.9 eV) obtained from photoconductivity measurement.[29] Another theoretical prediction that does not agree well with the experiment is the position of the LVB. These differences are discussed in Sec. IV.

We essentially follow Singh and Jarlborg[35] for the momentum density calculation. However, we do not include a so-called overlap correction arising from the calculation of the Fourier transform by integrating over the Wigner-Seitz spheres rather than the unit cell. This correction is computationally expensive to implement, especially for such a complex solid as α-quartz, and it does not produce a noticeable change to the electron-momentum density. Results of the momentum density calculations along three high-symmetry directions are shown in Fig. 3. We present the momentum densities together with the corresponding band energies plotted in the repeated zone scheme. In the LVB the momentum density is dominated by the s-like oxygen orbitals. In the UVB the momentum density is p-like and peaks away from the zero momentum. These features are fairly isotropic and can be clearly seen in the spherically averaged momentum density plots presented in Sec. IV.

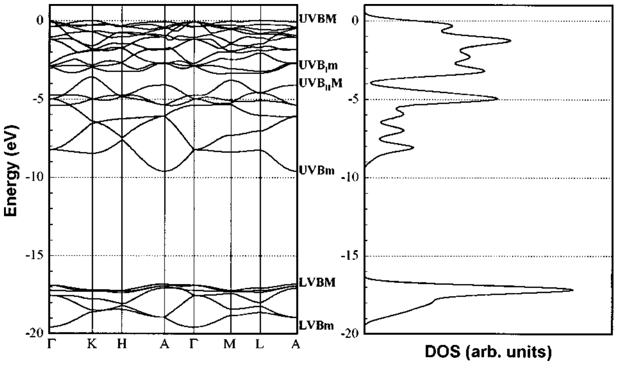

FIG. 2. The valence-band structure and DOS spectrum in α-quartz. Energy positions are labeled with M for maximum and m for minimum. The DOS spectrum has been convoluted with a Gaussian function of full width at half maximum of 0.5 eV. The peaks in the DOS reflect the complex band structure of α-quartz.

III. EXPERIMENTAL DETAILS

A. Sample preparation

The preparation of $(e,2e)$ samples is a challenging task. Details of the equipment and procedure used to prepare an $(e,2e)$ sample have been described elsewhere.[36] $(e,2e)$ spectroscopy requires ultrathin (~ 10 nm) free-standing membranes to minimize electron multiple scattering before and after an $(e,2e)$ event. For an insulating material such as SiO_2 it is necessary to have a conducting sublayer to avoid problems associated with sample charging. We have already established a successful procedure for preparing single-crystal Si samples; the SiO_2 sample is obtained by oxidizing the already thinned Si film. A brief description of the SiO_2 sample preparation is given below.

We use a commercial SIMOX wafer [200 nm Si (100)/ 400 nm SiO_2 on a Si substrate] as the starting material. We deposit another 400 nm SiO_2 on top of the wafer as a protective layer. The bulk Si substrate is removed in a chemical etching process that stops at the SiO_2 layer. A sandwich structure (400 nm SiO_2/200 nm Si/ 400 nm SiO_2) with a diameter of 0.5–1 mm is formed in middle of the sample. The SiO_2 layers are then removed in an HF dip. The remaining 200 nm Si membrane is further thinned by reactive plasma etching using an 80:20 mixture of CF_4 and O_2. Film thickness is constantly monitored by a laser beam interferometer[36] and the etching is stopped when the film is about 10 nm thick. The sample then undergoes 30 min of Ar sputter cleaning (400 eV, $\sim 2\ \mu\mathrm{A/mm^2}$) to remove all the surface contaminants. The clean surface is then exposed to an O_2 plasma for oxidation. The depth of the oxide layer is controlled by the exposure time and the bias voltage (100–200 V) applied to the sample. Subsequent annealing ensures good Si-O bonding. The Auger spectra shown in Fig. 4 indicate a typical SiO_2 surface with no observable contamination.

The thickness of the SiO_2 layer can only be estimated from the experimental results. As indicated later, our spectrometer is sensitive to a layer only 2–3 nm thick beneath the

TABLE II. Comparison of self-consistent band calculations for α-quartz. Energy positions indicated in Fig. 2 are relative to UVBM in eV and the corresponding high-symmetry points are indicated in the bracket.

Reference	Ref. 15	Ref. 12	Ref. 16	Ref. 14	Present
Calculation method	Mixed basis	Pseudo-potential	Pseudo-potential	LCAO	LMTO
Crystal symmetry	D_3^6	D_3^4	D_3^4	D_3^4	D_3^4
Conduction-band minimum	6.3(Γ)	9.2(Γ)	5.8(Γ)	5.59(Γ)	6.57(Γ)
UVBM	$0(A)$	$0(M)$	$0(K)$	$0(K)$	$0(K)$
UVB$_{\mathrm{I}}$m	$-3.6(H)$	$-4.3(K)$	$-3.4(H)$	$-3.50(L)$	$-3.30(M)$
UVB$_{\mathrm{II}}$M	$-6.1(K)$	$-5.7(K)$	$-4.7(K)$	$-5.07(K)$	$-3.59(K)$
UVBm	$-11.5(A)$	$-12.8(A)$	$-9.4(A)$	$-10.10(A)$	$-9.62(A)$
LVBM	$-21.0(H)$	$-24.8(H)$	$-16.9(A)$	$-17.42(A)$	$-16.87(A)$
LVBm	$-23.3(\Gamma)$	$-26.1(\Gamma)$	$-19.3(\Gamma)$	$-19.80(\Gamma)$	$-19.57(\Gamma)$

electron exit surface. The thickness of the SiO$_2$ layer must be greater than this value otherwise the Si sublayer becomes detectable. We also know the Si film is not totally oxidized since the target does not charge up from the incident beam. The uncertainty in SiO$_2$ thickness is not a serious problem in the $(e,2e)$ measurement as long as the Si sublayer signal is suppressed. However this does introduce some difficulties in data interpretation as described in Sec. IV.

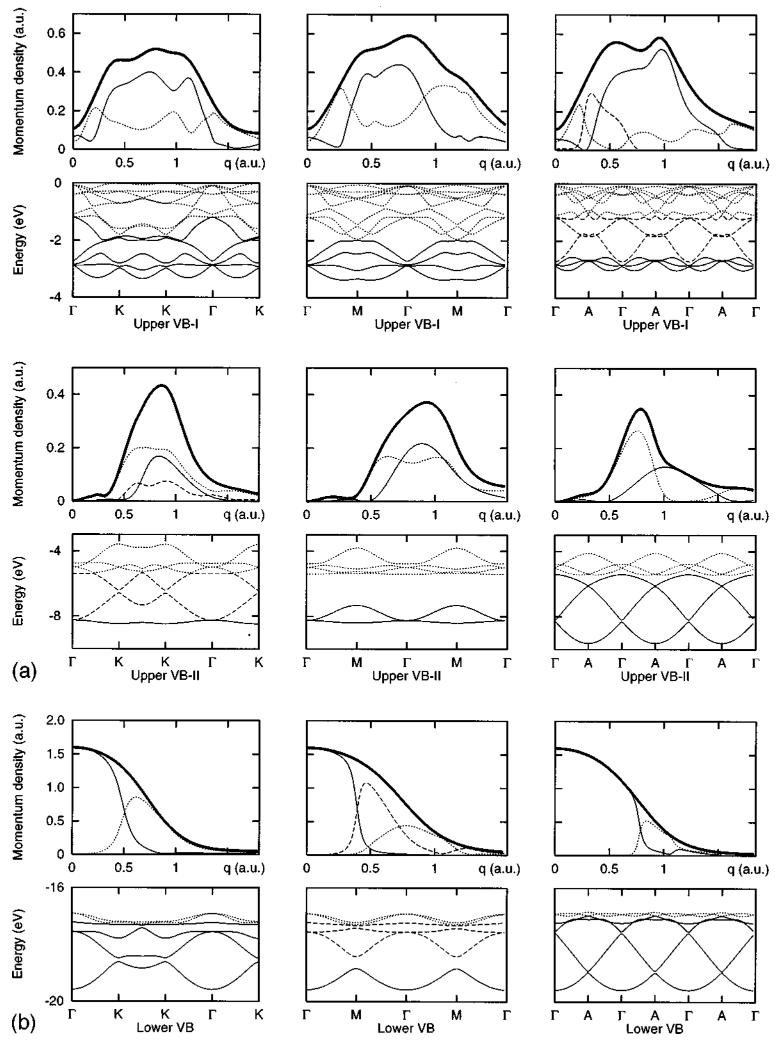

FIG. 3. The momentum densities and band energies for the UVB$_{\mathrm{I}}$ (top two rows), UVB$_{\mathrm{II}}$ (middle two rows), and LVB (bottom two rows) along the three main symmetry directions in α-quartz. The momentum density of several close bands is summed and represented by the same line-style as on the band-energy plot. The total momentum densities are shown as the bold lines.

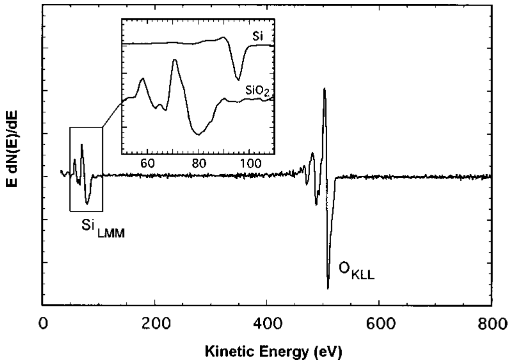

FIG. 4. The Auger spectrum for the oxidized Si film. The chemical shift of the Si LMM peak due to the Si-O bond is shown in the inset where the elemental Si LMM peak is included for comparison. A typical SiO_2 feature with no surface contamination is observed.

B. The (*e*,2*e*) measurement

The (*e*,2*e*) spectrometer has been described in detail by Storer *et al.*[37] The general principle of (*e*,2*e*) spectroscopy is also well documented in the literature.[2,5–10] In short, we use a transmission geometry as shown in Fig. 5 for the (*e*,2*e*) measurement. The energies and angles of the incident and scattered (fast 19.6 keV and slow 1.2 keV) electrons are indicated in the figure. These kinematics satisfy the Bethe ridge requirement, which means the momentum range we measure includes the origin of momentum space. The energy and momentum transfer in the (*e*,2*e*) event shown in Fig. 5 is large so the binary collision mechanism dominates the ionization process. We use two-dimensional position-sensitive detectors for both the fast and slow electron analyzers to detect a range of energies and azimuthal angles [shaded region in Fig. 5(a)] simultaneously. The energy window and detectable azimuthal angle range are 20 eV and ±18° for the fast electron and 36 eV and ±6° for the slow electron. Our spectrometer therefore covers an overall energy range of 56 eV with a resolution of 19 eV and an effective momentum range of 6.0 a.u. (−3.0 a.u. to 3.0 a.u.) with a resolution of 0.15 a.u. This parallel detection method allows us to complete the measurement within a few days in a vacuum of 1.2×10^{-10} Torr, hence minimizing the chance of surface contamination.

The asymmetric geometry shown in Fig. 5(b) brings in the surface-sensitive feature of our spectrometer. Since the escape depth of the slow electron (before it suffers an elastic or inelastic scattering, thus losing the information it carries) is about 2–3 nm below the exit surface [shaded layer in Fig. 5(b)], most (*e*,2*e*) signals come from this thin layer only. Although this layer is pretty thin, it has been found[10] that surface contributions can be safely neglected in the interpretation of the (*e*,2*e*) results. If the SiO_2 layer is thicker than this, the Si sublayer feature will not be observed. The Si sublayer which is needed as a conducting layer, however, as contributes to electron multiple scattering events that need to be minimized in the (*e*,2*e*) measurements.

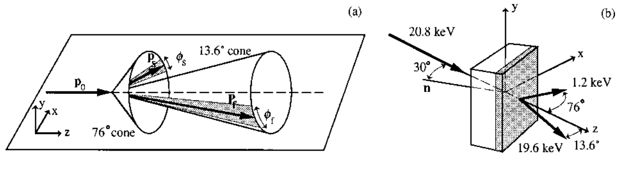

FIG. 5. The experimental setup in (*e*,2*e*) measurements. (a) The scattering geometry. The analyzers cover a range of azimuthal angles that select the target electron momenta in the *y* direction. (b) The beam energies of the incident and outgoing electrons and the target position relative to the incident beam.

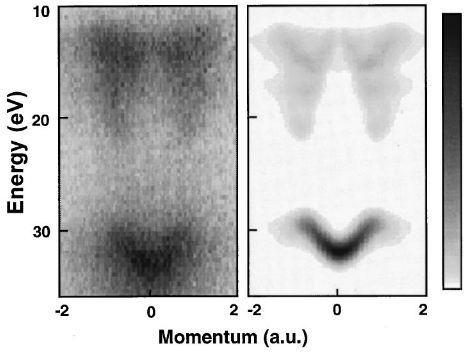

FIG. 6. The measured and calculated energy-momentum density of SiO_2. The energy scale is relative to the vacuum level of the spectrometer. The LMTO calculation has been convoluted with 1.5 eV energy width (FWHM). A linear gray scale is used to represent the variation in intensities. Darker scale corresponds to higher intensity.

IV. RESULTS AND DISCUSSION

In Fig. 6 we compare the energy-momentum density plot obtained from (*e*,2*e*) measurement and LMTO calculation. For illustration purposes the LMTO result has been convoluted with a 1.5-eV energy resolution to allow for finite lifetime effects and the experimental energy resolution, and aligned with the experiment at the valence-band maximum (UVBM). The experimental data show the UVBM is ~11 eV below the vacuum level and the width of the UVB is 10 eV. We see very good agreement in the shape and width of the UVB between theory and experiment. For the LVB the agreement between the experiment and LMTO calculation is not as good as for the UVB. The theoretical prediction of UVB-LVB gap is a little smaller than the experiment and is clearly shown in the following analysis.

We first present a detailed comparison between the experiment and LMTO calculation. In Fig. 7 we show the binding energy spectra for a series of momentum intervals (0.2 a.u. wide). At all momenta the experimental data show extra intensities which can be explained by multiple elastic scattering. If an electron changes its direction slightly due to elastic scattering it will end up at the wrong momentum position in the energy-momentum plot, smearing the picture. This process can be quantitatively simulated using the Monte Carlo method.[38] To perform this simulation, one needs to know the sample structure and thickness in advance. However due to the uncertainty of sample structure mentioned in Sec. III, we have not made such attempts. Nevertheless, the agreement between theory and raw data is in some respects satisfactory. For example, in the 0.6–0.8 a.u. plot, theory predicts three peaks in the UVB, which can also be seen in

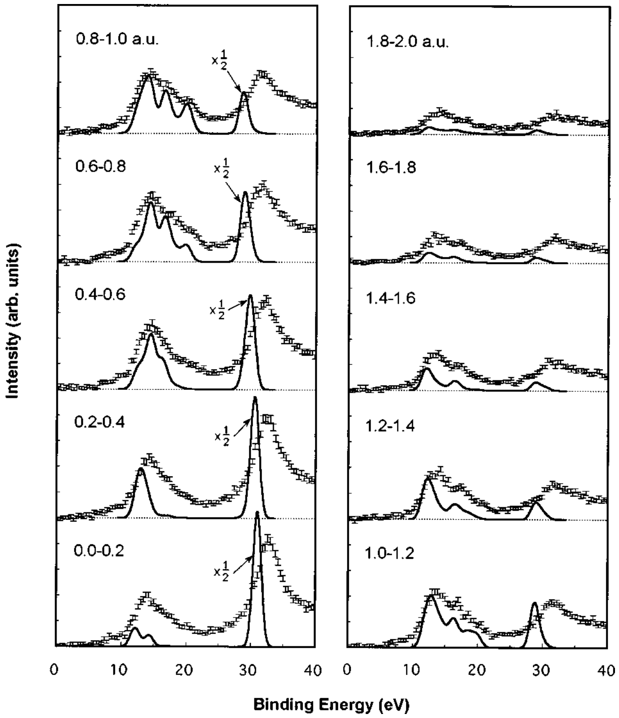

FIG. 7. The binding-energy spectra in momentum bins from 0.0 to 2.0 a.u. with a 0.2-a.u. bin width. The error bars are the raw experimental data and the solid lines are from the LMTO calculation. The LVB peaks in the LMTO calculation in the left panel (0.0–1.0 a.u.) are reduced by a factor of 2 for ease of comparison.

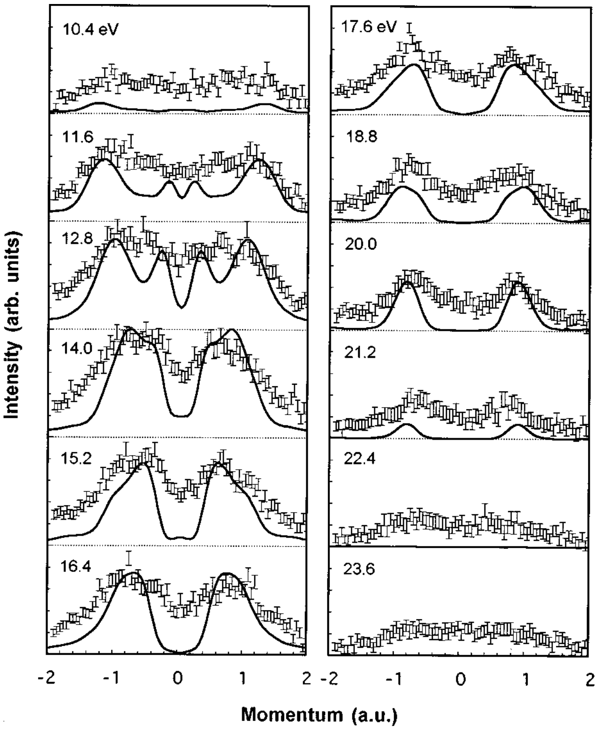

FIG. 8. The momentum distributions in binding-energy bins covering the entire UVB. The binding energies at the middle of the 1.2-eV-wide bins are shown in each plot. The error bars are the raw data and the solid lines are from the LMTO calculation.

the experiment. This happens for most plots shown in Fig. 7. The LVB peak predicted by theory is sharp and intense. We have reduced the theoretical LVB peak intensity by a factor of 2 in the left panel to give a clear picture. The differences in peak position and width is obvious. The dispersion of the LVB can be seen in Fig. 7 as the peak position shifts towards lower binding energies at higher momenta in both the data and the calculation.

Detailed comparison between theory and experiment has also been made in Figs. 8 and 9 where the energy-resolved momentum distributions for UVB and LVB are shown. In both figures the width of the energy bin is 1.2 eV and we use the middle energy to label the plot at the top-left corner (e.g., label 10.4 eV for 9.8–11.0 eV bin). The LMTO calculation is aligned at the UVBM (11.6 eV bin in Fig. 8) with the experiment. In Fig. 9, a 2 eV shift in binding energy has been added to the LMTO calculation so the theory predicts correct peak positions. In most of the plots, we see more intensity at zero and higher momenta due to multiple elastic scattering mentioned before. This smearing effect also causes the double peaks predicted by theory (in 11.6- and 12.8-eV bins) not to be clearly observed in the experiment. In the 22.4- and 23.6-eV bins, we still see some intensity that could be caused by inelastic scattering (such as plasmon excitation). This effect is probably also responsible for the nonzero intensities in Fig. 7 between UVB and LVB and below the LVB peak. A deconvolution procedure described elsewhere (see, for example, Ref. 10) has been carried out on the experimental data to remove contributions from plasmon excitations. This procedure reduces the intensities in the 22.4- and 23.6-eV bins in Fig. 8 and 34.6–37.0 eV bins in Fig. 9 by a factor of 2. For two reasons we have not included the deconvoluted data in the plots. One is that the deconvolution procedure does not include elastic scattering, which combines with the momentum resolution to further broaden the peaks shown in

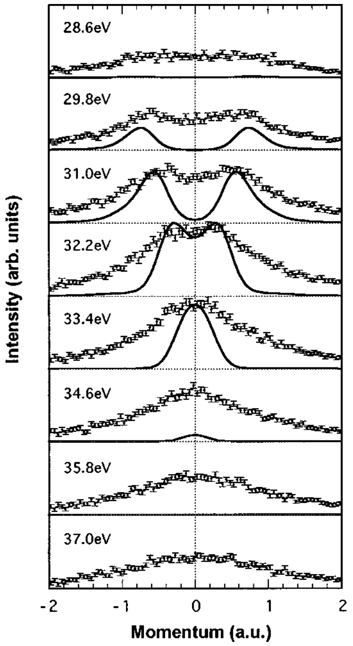

FIG. 9. The momentum distributions in binding-energy bins covering the entire LVB (details as in Fig. 8). The theoretical curves are shifted towards higher binding energies by 2 eV to compare with the experiment.

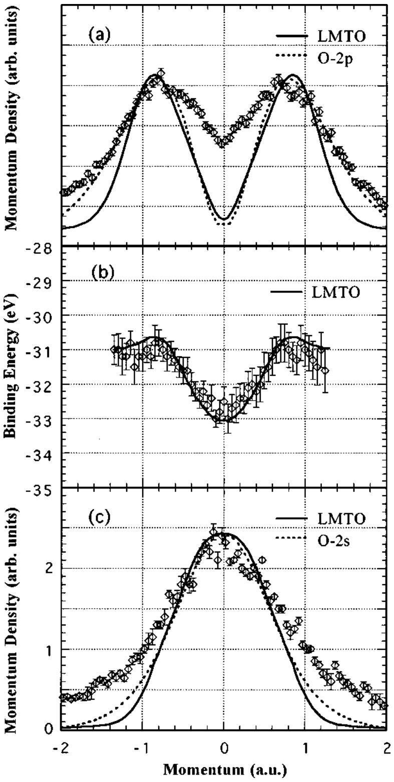

FIG. 10. (a) The measured and calculated momentum distributions of the entire UVB. (b) The dispersion in the LVB. The LMTO calculation has been shifted by 2 eV to higher binding energies. (c) The measured and calculated momentum distributions of LVB. The momentum distributions of atomic O 2s and O 2p orbitals are included for comparison.

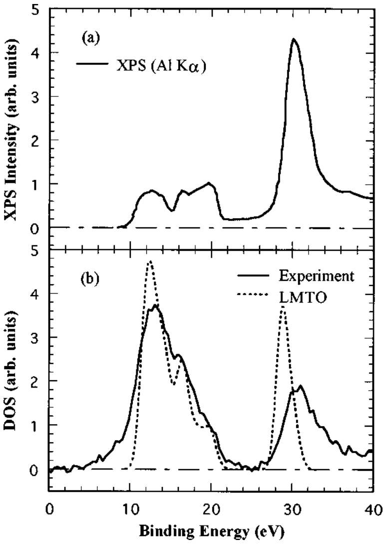

FIG. 11. (a) The XPS data (from Ref. 23) for amorphous SiO_2. (b) The DOS spectra from q^2-weighted integration of the data shown in Fig. 6 over the momentum range of -2 to 2 a.u. A deconvolution procedure has been carried out to remove the contributions from plasmon excitations. The total area of the theoretical curve is kept the same as the experimental one.

Figs. 8 and 9, but whose effect is not significant to invalidate the momentum density conclusions. The other reason is that we consider multiple scattering part of the experimental data and the discrepancies between raw data and theory are expected. The deconvolution procedure is, however, needed for more detailed data analysis (e.g., to create the DOS spectrum in Fig. 11). The quality of the experimental data allows a successful deconvolution as the nonzero intensities (between UVB and LVB and below LVB) drop to zero after deconvolution as expected.

In Figs. 7–9 the experimental data generally follow the LMTO results in shape and intensity, confirming a good agreement between the theory and experiment. In Figs. 10 and 11 the experimental data are further analyzed to reveal more information contained in the (e,2e) data. In Fig. 3 the LMTO calculation predicts p-like and s-like momentum densities in UVB and LVB, respectively. These densities are fairly isotropic and change little after spherically averaging. In Fig. 10(a), the momentum density of the UVB (sum of the plots shown in Fig. 8) is plotted and a p-like feature is seen. The momentum distribution of atomic O 2p orbital is also shown for comparison. The O 2p distribution is broader than the LMTO result and if further broadening effects (due to elastic scattering) are introduced, the LMTO result would be a closer match to the experiment.

In Fig. 10(b) we plot the LVB peak position for different momentum values. The data clearly show a 2-eV dispersion. The LMTO result has been shifted by 2 eV to enable a detailed comparison. In spite of the 2-eV shift, the dispersion of the LVB is well predicted by the LMTO calculation. In Fig. 10(c) the LVB peak intensity is plotted as a function of momentum together with the theoretical momentum densities. The momentum density of atomic O 2s state differs little from the LMTO calculation and experiment, indicating a corelike feature in LVB.

One can see that the information contained in Fig. 7 is more complete than the DOS. However in the literature the DOS spectra are more common since it is often compared to angle-integrated photoemission spectra. In Fig. 11(a) we show a photoemission spectrum[23] (using Al $K\alpha$ emission) for amorphous SiO_2. We see that the LVB peak area is much larger than the UVB peak area due to an enhanced photoemission cross section in the LVB. The photoemission cross section for atomic O 2s state is about 7.3 times larger than that for O 2p state according to Scofield.[4] A similar enhancement effect obviously exists in SiO_2 as well. The peak intensity in Fig. 11(a) cannot be related to DOS intensity unless the cross section is known. However, because the (e,2e) cross section is a direct measure of valence-band occupation, it leads to a DOS spectrum without such enhancement. This is clearly demonstrated in Fig. 11(b) where the DOS spectra for both the (e,2e) measurement and LMTO calculation are shown. These spectra are obtained by performing a q^2-weighted integration over the -2 to 2 a.u. momentum range. A deconvolution process mentioned before is carried out prior to the integration so the intensities between the UVB and LVB and below LVB are reduced to zero. Sarnthein, Pasquarello, and Car[30] calculated the DOS for glass at 300 K, which agrees very well with our resultSince there are 18 bands in the UVB and 6 bands in the LVB, the ratio of the UVB peak area and LVB peak area should be 3. We obtain a ratio of 2.8 in Fig. 11(b) for both theory and experiment and the small discrepancy may be .

caused by the limited momentum integration range. This UVB/LVB ratio may be slightly affected if the elastic scattering is taken into account. A rough estimation indicates that if one increases the theoretical peak width by 10% to accommodate the broadening effect caused by elastic scattering the UVB/LVB ratio would be reduced by 15%.

Elastic-scattering corrections would not affect the good agreement in the shape and width of UVB observed in Fig. 11(b). The 10-eV-wide UVB contains three distinguishable intensity maxima at 13, 16, and 19 eV below the vacuum level. Unlike the DOS shown in Fig. 2, which has many peaks in UVB due to small energy width (0.5 eV) included, the calculated DOS shown in Fig. 11(b) with the 1.5-eV energy width included, has only three peaks that fit the experimental result nicely. In the LVB however, the experimental peak is 4 eV wide [full width at half maximum (FWHM)] while the LMTO prediction for the peak width is only 2 eV (including the 1.5 eV energy width). The LVB peak position is 31 eV below the vacuum level. This result agrees well with the photoemission and electron energy-loss experiments,[23,24] which indicate that the LVB peak is located ~20 eV below the UVB maximum. Like other theoretical predictions,[11,14,16] the LMTO calculations show that the energy separation between the UVB maximum and the LVB peak is smaller than the experimental value. We believe some physical mechanisms that are not included in the one-electron band-structure calculation play a role here. It has been indicated[16] that in XPS the difference in the energy position of core and valence states is several eV larger than the difference between the calculated one-electron energy levels, due to electron-hole interaction. The independent particle approximation may not be adequate to describe the corelike O 2*s* states in SiO_2.

Finally we compare the energy-momentum density plots for SiO_2 and Al_2O_3 (from Ref. 10) in Fig. 12. Both materials are insulators and the valence band for each of them contains a *p*-like UVB and a *s*-like LVB. In Fig. 12 we see the dispersion in UVB and LVB is larger in SiO_2 and this may be related to the interatomic distance in these two materials (1.98 Å for the Al-O bond and 1.61 Å for the Si-O bond). An increased overlap of the wave functions is generally expected to increase the dispersion. We concentrate on the valence-band maximum (UVBM) first. Closer inspection of Fig. 6 and Fig. 12 shows that the UVBM in SiO_2 is not completely flat. Also in the 10.4- and 11.6-eV plots in Fig. 8, we see more intensity at higher momenta that supports this claim. The binding energy is slightly higher at zero momentum than at the higher momenta ($\sim\pm1$ a.u.). This indicates an indirect band gap and a large hole effective mass at the UVBM, which agrees with other observations.[27] In Al_2O_3 the UVBM is relatively flat which agrees with the theoretical description of the UVBM for a direct band gap and ''huge'' hole effective mass.[39]

The energy position of the UVBM is about 1 eV lower in SiO_2 than that in Al_2O_3. Since (*e*,2*e*) spectroscopy cannot pinpoint the unoccupied conduction-band position, the data shown in Fig. 12 give little hint to the size of the band gap. Gritsenko, Ivanov, and Morokov[27] claimed that in amorphous SiO_2 the bottom of conduction band is only 1.0 eV below the vacuum level and from the photoemission data on the potential barrier for holes on the Si-SiO_2 boundary (about 4 eV), the UVBM should be 9.0 eV below the vacuum level. Our result (~11 eV below the vacuum level) is more reliable as the energy scale of our spectrometer is well calibrated.[37] Detailed analysis[14] indicates that the optical data[28] could underestimate the band gap due to the formation of exciton. This means the UVBM should be lower which agrees with our result. However the discrepancy between the theoretical band gap (6.6 eV in LMTO calculation) and the optical band gap[29] (8.9 eV) is a well-known problem. It has been argued that the discrepancy would be much smaller because direct transitions at or near Γ are symmetry forbidden.[14] A detailed discussion on this issue is beyond the scope of this paper.

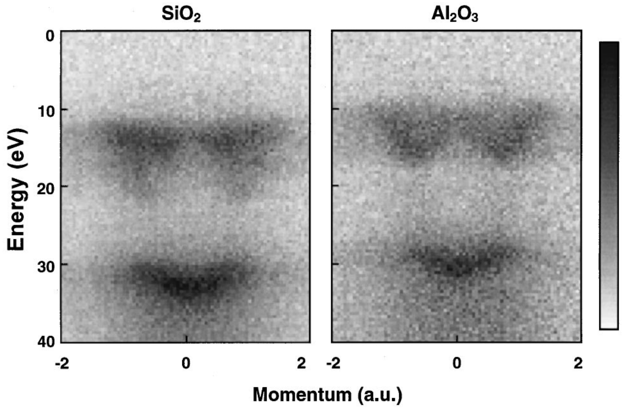

FIG. 12. The measured energy momentum densities for SiO_2 and Al_2O_3 (from Ref. 10) obtained from (*e*,2*e*) spectroscopy. The binding energy is relative to the vacuum level of the spectrometer, which is properly calibrated as described in Ref. 37. The binding energy and gray scale used here are the same as in Fig. 6.

V. CONCLUSIONS

We have measured the energy-momentum density of amorphous SiO_2 using (*e*,2*e*) spectroscopy. We found that the valence-band maximum is about 11 eV below the vacuum level and is not totally flat. Three peaks locatedaround 13, 16, and 19 eV below the vacuum level are found in the 10 eV-wide *p*-like UVB, which is separated from the LVB maximum by 9 eV. The LVB is *s*-like with a 2-eV dispersion. These features are reproduced in the LMTO calculation using α-quartz as the model crystal. Except for the width and position of LVB, the measured energy-momentum density agrees very well with the LMTO calculation. Our results show that short-range order within the SiO_2 family actually determines the electronic structure of the material.

ACKNOWLEDGMENTS

We would like to thank Dr. O. Reinhold of DSTO for his assistance in the Si sample preparation. We also acknowledge Professor O. Jepsen of Max-Planck-Institut für Festkörperforschung for placing the latest version of the LMTO code at our disposal. The study of the electronic structure of solids using (*e*,2*e*) spectroscopy is supported by the Australian Research Council.

[1] I. E. McCarthy and E. Weigold, Rep. Prog. Phys. **54**, 789 (1991).

[2] M. Vos and I. E. McCarthy, Rev. Mod. Phys. **67**, 713 (1995).

[3] V. G. Levin, V. G. Neudatchin, and Yu. F. Smirnov, Phys. Status Solidi B **49**, 489 (1972).

[4] J. H. Scofield, J. Electron Spectrosc. Relat. Phenom. **8**, 129 (1976).

[5] M. Vos, P. Storer, Y. Q. Cai, I. E. McCarthy, and E. Weigold, Phys. Rev. B **51**, 1866 (1995).

[6] M. Vos, P. Storer, Y. Q. Cai, A. S. Kheifets, I. E. McCarthy, and E. Weigold, J. Phys.: Condens. Matter **7**, 279 (1995).

[7] Y. Q. Cai, M. Vos, P. Storer, A. S. Kheifets, I. E. McCarthy, and E. Weigold, Phys. Rev. B **51**, 3449 (1995).

[8] X. Guo, Z. Fang, A. S. Kheifets, S. A. Canney, M. Vos, I. E. McCarthy and E. Weigold, Phys. Rev. B (to be published).

[9] S. A. Canney, M. Vos, A. S. Kheifets, N. Clisby, I. E. McCarthy, and E. Weigold, J. Phys.: Condens. Matter **9**, 1931 (1997).

[10] X. Guo, S. A. Canney, A. S. Kheifets, M. Vos, Z. Fang, S. Utteridge, I. E. McCarthy, and E. Weigold, Phys. Rev. B **54**, 17 943 (1996).

[11] A. Di Pomponio and A. Continenza, Phys. Rev. B **48**, 12 558 (1993); **50**, 5950 (1994); **54**, 13 687 (1996); A. Di Pomponio, A. Continenza, L. Lozzi, M. Passacantando, S. Santucci, and P. Picozzi, Solid State Commun. **95**, 313 (1995).

[12] J. R. Chelikowsky and M. Schlüter, Phys. Rev. B **15**, 4020 (1977).

[13] W. Y. Ching, Phys. Rev. B **26**, 6610 (1982); **26**, 6622 (1982); **26**, 6633 (1982).

[14] Y. N. Xu and W. Y. Ching, Phys. Rev. B **44**, 11 048 (1991).

[15] E. Calabrese and W. B. Fowler, Phys. Rev. B **18**, 2888 (1978).

[16] N. Binggeli, N. Troullier, J. L. Martins, and J. R. Chelikowsky, Phys. Rev. B **44**, 4771 (1991).

[17] D. C. Allen and M. P. Teter, Phys. Rev. Lett. **59**, 1136 (1987).

[18] F. Liebau, in *The Physics and Technology of Amorphous* SiO_2, edited by R. A. B. Devine (Plenum, New York, 1988).

[19] R. W. G. Wyckoff, *Crystal Structures* (Interscience, New York, 1965).

[20] F. Liu, S. H. Garofalini, R. D. King-Smith, and D. Vanderbilt, Phys. Rev. Lett. **70**, 2750 (1993).

[21] S. Ciraci and I. P. Batra, Phys. Rev. B **15**, 4923 (1977); S. Ciraci and S. Ellialtioglu, *ibid.* **25**, 4019 (1982); P. M. Schneider and W. B. Fowler, *ibid.* **18**, 7122 (1978).

[22] R. J. Powell and M. Morad, J. Appl. Phys. **49**, 2499 (1978).

[23] B. Fischer, R. A. Pollak, T. H. DiStefano, and W. D. Grobman, Phys. Rev. B **15**, 3193 (1977).

[24] H. Ibach and J. E. Rowe, Phys. Rev. B **10**, 710 (1974).

[25] G. Wiech, Solid State Commun. **52**, 807 (1984).

[26] V. J. Nithianandam and S. E. Schnatterly, Phys. Rev. B **15**, 5547 (1988).

[27] V. A. Gritsenko, R. M. Ivanov, and Yu. N. Morokov, Zh. Eksp. Teor. Fiz. **108**, 2216 (1995); [Sov. Phys. JETP **81**, 1208 (1995)].

[28] H. R. Phillip, in *Handbook of Optical Constants of Solids*, edited by E. D. Palik (Academic, Orlando, 1985).

[29] T. H. DiStefano and D. E. Eastman, Solid State Commun. **9**, 2259 (1971).

[30] J. Sarnthein, A. Pasquarello, and R. Car, Phys. Rev. B **52**, 12 690 (1995).

[31] H. L. Skriver, *The LMTO Method* (Springer-Verlag, Berlin, 1984).

[32] A. S. Kheifets and Y. Q. Cai, J. Phys. C **7**, 1821 (1995); A. S. Kheifets and M. Vos, *ibid.* **1**, 3895 (1995).

[33] L. Levien, C. T. Prewitt, and D. J. Weidner, Am. Mineral. **65**, 920 (1980).

[34] G. Krier, O. Jepsen, A. Burkhardt, and O. K. Andersen, *The TB-LMTO ASA Program* (Max-Planck-Institut für Festkörperforschung, Stuttgart, 1994).

[35] A. K. Singh and T. Jarlborg, J. Phys. F **15**, 727 (1978).

[36] Z. Fang, X. Guo, S. Utteridge, S. Canney, I. E. McCarthy, M. Vos, and E. Weigold, Rev. Sci. Instrum. **68**, 4396 (1997).

[37] P. Storer, R. S. Caprari, S. A. C. Clark, M. Vos, and E. Weigold, Rev. Sci. Instrum. **65**, 2214 (1994).

[38] M. Vos and M. Bottema, Phys. Rev. B **54**, 5946 (1996).

[39] Y. Xu and W. Y. Ching, Phys. Rev. B **43**, 4461 (1991).